

Experimental demonstration of high compression of space by optical spaceplates

Ryan Hogan,^{1,*} Yaryna Mamchur,¹ R. Margoth Córdova-Castro,¹ Graham Carlow,²
Brian T. Sullivan,² Orad Reshef,¹ Robert W. Boyd,^{1,3} and Jeff S. Lundeen¹

¹Nexus for Quantum Technologies, Department of Physics,
University of Ottawa, Ottawa, K1N 6N5, ON, Canada

²Iridian Spectral Technologies, Ottawa, ON, Canada

³University of Rochester, Institute of Optics, Rochester, New York, 14627, USA

The physical size of optical imaging systems is one of the greatest constraints on their use, limiting the performance and deployment of a range of systems from telescopes to mobile phone cameras. Spaceplates are nonlocal optical devices that compress free-space propagation into a shorter distance, paving the way for more compact optical systems, potentially even thin flat cameras. Here, we demonstrate the first engineered optical spaceplate and experimentally observe the highest space compression ratios yet demonstrated in any wavelength region, up to $\mathcal{R} = 176 \pm 14$, which is 29 times higher than any previous device [1]. Our spaceplate is a multilayer stack, a well-established commercial fabrication technology that supports mass production. The versatility of these stacks allows for the freedom to customize the spaceplate's bandwidth and angular range, impossible with previous optical experimental spaceplates, which were made of bulk materials. With the appropriate choice of these two parameters, multilayer spaceplates have near-term applications in light detection and ranging (LIDAR) technologies, retinal scanners, endoscopes, and other size-constrained optical devices.

Introduction

As the demand for more compact optical imaging systems grows, new approaches to shrinking their physical footprint have become essential. Until recently, research has focused mainly on reducing the thickness of optical elements, with notable progress in metasurfaces [2], diffractive lenses [3, 4], and refractive Fresnel lenses [5]. However, shrinking these elements [6, 7] only addresses one part of the challenge of optical miniaturization: the propagation of light across the physical distance between elements is equally important for image formation. These distances must also be reduced to compactify the entirety of an optical system, such as a telescope or microscope. Ref. [8, 9] proposed a new approach to reducing the total length of optical systems, “the spaceplate”: a nonlocal optical device that compresses the propagation of light.

As shown in Fig. 1a, a spaceplate can be understood by its action on incoming rays of light. A ray incident at angle θ will propagate through an air path of length d_{eff} (i.e., a slab of free space), exit at the same angle θ , and be displaced transversely by distance $w = d_{\text{eff}} \tan \theta$ by simple geometry. The spaceplate provides precisely this transformation but in a shorter length d and, in this sense, compresses the needed space by the ratio $\mathcal{R} = d_{\text{eff}}/d$ [8].

Consider the effect of the spaceplate on the rays focused by a lens, as shown in Fig. 1b. The transverse ray displacement w removes the need for d_{eff} of propagation length after the lens. With the spaceplate thickness d still present, the distance between the lens and the focus is reduced by $\Delta = d_{\text{eff}} - d$. Typically, one would shorten the distance to the focus by simply reducing the lens's focal length; however, doing this would be

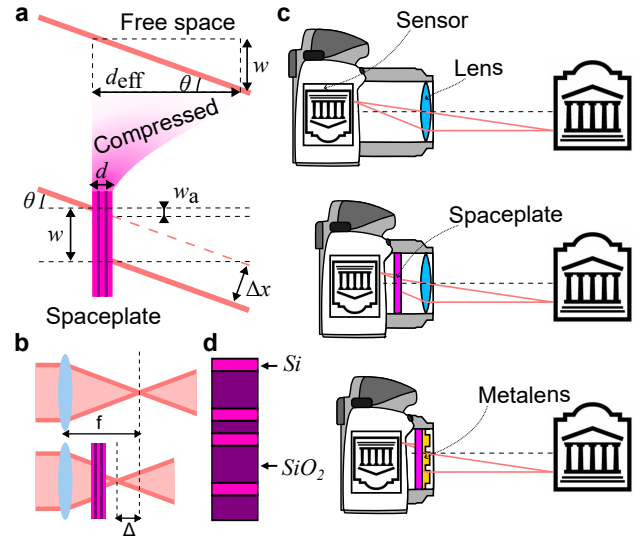


FIG. 1. The action of a spaceplate. **a.** An effective length of free space, d_{eff} , is replaced by a spaceplate of a thickness, d . In both cases, for light incident at angle θ , the beam is shifted by w , resulting in a lateral shift Δx . **b.** When the spaceplate is placed in front of a lens, the focal plane experiences a shift $\Delta = d_{\text{eff}} - d$ towards the device. **c.** With the use of both a metalens and a spaceplate, flat and thin optical systems are possible. **d.** A unit cell of multilayer spaceplate sample FCP2, alternating between hydrogenated amorphous silicon (Si) and silica (SiO_2).

accompanied by a change in the ray angles that changes image magnification, which may not be desired. In contrast, adding a spaceplate to a camera will not change its magnification. In this way, the spaceplate breaks the link between magnification and focal length and thus relaxes the limitations on all dimensions of an imaging system. For example, combining the spaceplate with a flat lens opens the path to the creation of a thin flat monolithic camera (see Fig. 1c) [8].

* ryan.hogan.j@gmail.com; Currently at National Key Laboratory of Solid State Microstructures, School of Physics, and Collaborative Innovation Center of Advanced Microstructures, Nanjing University, Nanjing, Jiangsu, 210093, China.

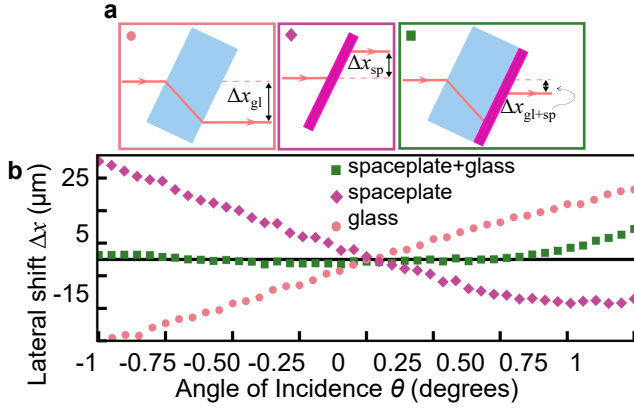


FIG. 2. Demonstration of a thin spaceplate cancelling the lateral beam shift created by a tilted glass plate **a.** A positive lateral shift due to refraction in a glass plate (left) versus a negative shift from a freestanding spaceplate (middle), and our measurement scenario: a multilayer spaceplate deposited on glass (right). **b.** Experimentally measured lateral shift for FPC2 at the wavelength of $\lambda = 1532.905$ nm for scenarios: **a-left**, Δx_{gl} (pink circles); **a-right**, Δx_{gl+sp} (green squares); and **a-middle**, the difference in their shifts, $\Delta x_{gl+sp} - \Delta x_{gl} = \Delta x_{sp}$ (purple diamonds). i.e., the lateral shift from the spaceplate alone. Notably, the green curve indicates almost no beam movement as the angle is changed, implying that the spaceplate is fully negating the lateral shift of the 260 times thicker glass.

Since their conceptual introduction and first experimental demonstration, spaceplates have attracted significant interest and innovation. Proposed theoretical design methodologies for engineered spaceplates include inverse design of multilayer stacks [8, 10], coupled resonators [11], and photonic crystals [9, 12]. Theoretical limits on the performance of spaceplates have also been studied [13, 14]; Ref. [13] showed that a spaceplate that operates throughout the visible spectrum and is made from physically realizable materials might achieve an \mathcal{R} as high as 8 up to a maximum angle of incidence θ_{\max} of 90° [13]. Two types of spaceplates have been experimentally demonstrated in the visible and near-infrared wavelength region, both composed of bulk crystals or optics; the first demonstration of the spaceplate concept only replaced space in an $n > 1$ medium [8], while the second replaced on order of a meter of vacuum propagation but only up to a small θ_{\max} ($\mathcal{R} < 15.6$ and $\theta_{\max} < 3.4^\circ$) [15]. An engineered high-compression-ratio spaceplate has been experimentally demonstrated solely in the microwave region (using a multilayer design with $\mathcal{R} < 6$ and $\theta_{\max} = 19.5^\circ$) [1]. For imaging purposes or use in integrated photonics, a spaceplate operating in the optical wavelength region would be desirable.

This work presents a multilayer spaceplate engineered to achieve high compression ratios in the optical wavelength region. As a first example that demonstrates its unusual action of reducing the propagation length, consider a light beam transmitted through a glass plate. The beam will move from side to side as the glass is tilted back and forth. On the other hand, as Fig. 2a shows, a spaceplate will move a beam in the opposite direction to that expected of the glass or any ordi-

nary material. In Fig. 2b, we present such experimental observations on a spaceplate with $\mathcal{R} = 96$. In particular, we show that this \mathcal{R} is so large that even though the spaceplate is only 11.51 microns thick, when placed on top of a 3-mm-thick glass plate, it cancels the beam movement despite being 260 times thinner. We present other similarly striking observations in more detail in the Results section.

We experimentally demonstrate two types of multilayer designs near a wavelength of 1550 nm made from alternating layers of silica (SiO_2 , $n = 1.44$) and amorphous silicon (deposited with hydrogen, a-Si:H, $n = 3.2$), which are common materials that are compatible with volume manufacturing in commercial fabrication facilities for multilayer stacks. We design the multilayer to create the nonlocal phase response associated with the Fourier transfer-function of free space [16]. A closely related nonlocal response, namely an angle-dependent phase shift, has long been shown to cause a transverse beam shift w [17], with some optical multilayer devices exhibiting large shifts [18, 19]. However, a spaceplate is defined not merely by its ability to cause a beam shift but by its capacity to produce this shift with the angular dependence required to replace free space, $w = d_{\text{eff}} \tan \theta$ (as shown in Fig. 1a).

Our two types of multilayer designs use different algorithms for choosing the layer thickness to achieve the spaceplate response. The first design (GD) is an inversely-designed aperiodic structure found from gradient-descent optimization as detailed in [10]. The second design (FPC) is a periodic structure consisting of a series of identical Fabry-Pérot cavities separated by $\lambda/2$ layers, motivated by [11]. (Note that the, the FPC design is distinct from the standard Fabry-Pérot filter design, which use $\lambda/4$ coupling layers between the cavities.) Due to the versatility of the multilayer platform, designs can be tuned to achieve a specific angular range, bandwidth, or compression ratio, although there are trade-offs between these performance parameters [13]. This design versatility makes multilayer spaceplates suitable for a wide range of applications, including LIDAR [20] and advanced imaging techniques [22, 23].

Results

Observation of the focal shift.

The most compelling application of spaceplates is for miniaturizing imaging systems. In this section, we observe the shortening of image and focal distances due to the presence of a spaceplate. All four of our multilayer structures, which range from 2.48 to 13.42 microns thick, are deposited on fused-silica glass substrates that are nominally 3 mm thick (exact numbers are given in the SI). While free-standing multilayer structures are possible, for this proof-of-principle demonstration, the thick glass simplifies fabrication and resists bending from the mechanical stress applied by the layers, which could add its own focus and change the magnification. However, the glass substrate complicates isolating the effect of the spaceplate since glass creates focal and lateral shifts opposite to those of a spaceplate. We find the shift due to the multilayer stack alone by measuring and subtracting the shift

created by a bare glass substrate of identical thickness, as described in the caption of Fig. 2b.

We start by applying the above method to measure the focal shift caused by a spaceplate. In Fig. 3a, we present measurements of the location of the focus of a beam that has traveled through a lens and then a spaceplate, similar to what is depicted in Fig. 1b. The 1550 nm wavelength beam has a Gaussian spatial profile and is focusing with an angular width of 1 degree. We find the focus's location along the propagation direction z by recording the $x - y$ spatial intensity distribution at a sequence of z positions using a camera. In Fig. 3a, we plot the spatial width ω along the x direction found from these distributions. The minimum width, i.e., the beam waist, marks the position of the focus, which we find by fitting to a standard hyperbolic relation for a Gaussian beam [16]. We define the location of the focus with nothing in the beam's path as $z = 0$. When only the glass piece is in the pathway of the beam, it comes to a focus at $z = 1.07$ mm, which is further from the lens, as expected for a medium with $n > 1$. On the other hand, when the spaceplate on glass is present, the beam focuses at $z = 0.57$ mm, implying that the 11.51 μm -thick spaceplate shortens the focal distance by 0.50 mm.

While the advance of a focusing beam provides a quantitative demonstration of the spaceplate effect, the more relevant aspect is its action on more structured fields, such as those present in imaging. For this purpose, a 100 x 100 μm^2 square section of a glass plate lithographically patterned with a gold structure was imaged. We chose a region containing a defect in the lithography as the imaging object. The gold-defect object is illuminated by the 1550 nm laser and imaged with a lens with diameter of 25.4 mm, the focal distance of $f = 50$ mm and a magnification of 1.53. We show camera images recorded at the three focal positions found for each scenario described above in Fig. 3b. The sharpest image for free space is found at $z = 0$, while glass only is $z = 1.07$ mm, and spaceplate on glass at $z = 0.57$ mm. This advancement was expected from the beam waist measurements and the image has no apparent magnification. We thereby observe the demonstration of the compactification of an imaging system by the spaceplate.

A comparison of the performance of the different spaceplate designs.

We test and compare four spaceplate devices, two based on the gradient-descent design (GD1 and GD2) and two based on the Fabry-Perot design (FPC1 and FPC2). In order to explore performance trade-offs, the GD1 and FPC1 devices were designed to have a larger θ_{max} than the GD2 and FPC2 devices. We investigate whether this higher angular range comes at the expense of bandwidth and compression ratio. We detail below how we characterize these performance parameters and discuss select results. A summary of the design and measured characteristics for each device is given in Table I.

The most accurate way to determine the compression ratio \mathcal{R} achieved by each device is to use the method shown in Fig. 2a and b. As depicted in Fig. 1a, the lateral beam shift [8]

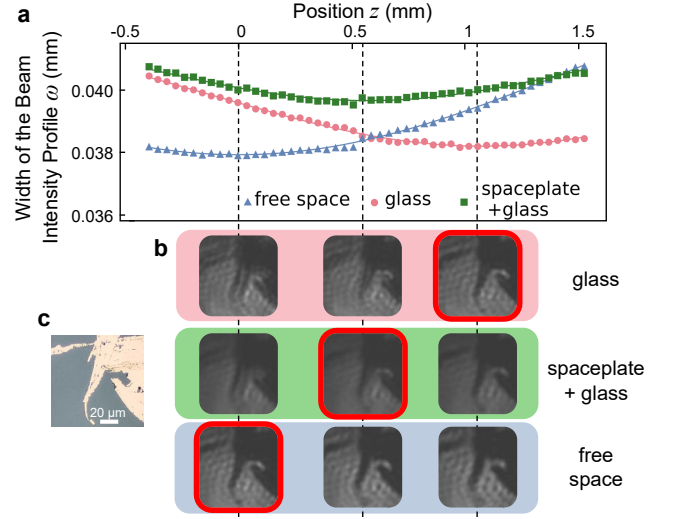


FIG. 3. Shifts of the focal plane and imaging. **a.** The width ω of a focusing beam with wavelength $\lambda = 1546.85$ nm, as in Fig. 1b, at different positions z along the beam propagation direction for free space (blue triangles), a spaceplate FPC2 on glass (green squares), and only glass (pink circles), along with a corresponding fitted curve from standard Gaussian beam theory (eq. 3.1-8 [16]). The minimum width is at the focus position (dashed vertical line), with the free space focus position taken as $z = 0$. Taking the difference between the focal position of the glass and spaceplate on glass cases shows that the spaceplate retracts the focus by 0.50 mm, equivalent to $\mathcal{R} = 43$. **b.** For each of the above three cases, a lithographic defect comprised of gold on glass, shown in **c**, was imaged at each of the focal positions found from **a**. For the spaceplate case, the sharp middle image indicates that this is indeed the image plane, demonstrating that the imaging system has been effectively shortened by 0.50 mm.

is given by

$$\Delta x = -(\mathcal{R} - 1)d \sin \theta. \quad (1)$$

Fig. 4a shows the measurement of Δx due to the spaceplate alone for all four devices. For each, the shift follows Eq. 1, increasing with angle up to a limiting angle, above which the shift gradually decreases to zero. This limiting angle defines the maximum angle of incidence θ_{max} of the spaceplate device, which is indicated by the shaded area for GD1 as an example. In the small-angle approximation, Eq. 1 for the lateral shift is a line, $\Delta x \approx -\theta \mathcal{R} d$. We fit this line to the measured beam shift up to the limiting angle thereby finding an experimental value for \mathcal{R} for each device. Both the small and large θ_{max} variants of either the GD or FPC designs exhibited the expected lateral shift of a spaceplate. That is, the shift increased linearly with angle and was in the opposite direction to the shift created by glass. The multilayer spaceplates feature frequency resonances over which both the transmission and the compression will vary. The GD designs have a single narrow resonance peak around the designed wavelength (Fig. 4c), while the FPC designs feature multiple peaks, each with different peak compression ratios (Fig. 4b). To determine the spectral bandwidth of the devices, we measure the trans-

Device	Thickness (μm^2)	Maximum Angle of Incidence θ_{max}	FWHM Bandwidth (nm)	Wavelength (nm)	Max Compression Ratio \mathcal{R}	Transmission (%)
FPC2	12.04	1°	0.143 \pm 0.004	1532.9	96 \pm 2	17
FPC2	12.04	1°	0.282 \pm 0.006	1546.85	41.9 \pm 0.6	11
FPC2	12.04	1°	0.147 \pm 0.005	1560.1	48.6 \pm 1.4	42
GD1	3.55	10°	2.8 \pm 0.3	1561.66	60 \pm 4	6
GD2	14.48	1°	0.055 \pm 0.007	1566.06	176 \pm 14	73
FPC1	13.10	3.5°	*	1579.8	3.4 \pm 0.3	5

TABLE I. **Summary of the performance characteristics for spaceplate devices GD1, GD2, FPC1, and FPC2.** For FPC2, we include values for each spectral response peak shown in 4b. The maximum compression factor and its uncertainty are respectively the mean and standard error over six trials. The wavelength and transmission noted here are recorded at the maximum compression ratio \mathcal{R} , the bandwidth is the peak’s spectral width, while the maximum angle of incidence θ_{max} is from the device design. (*) Only the peak compression ratio was extracted for FPC1 before the device malfunctioned.

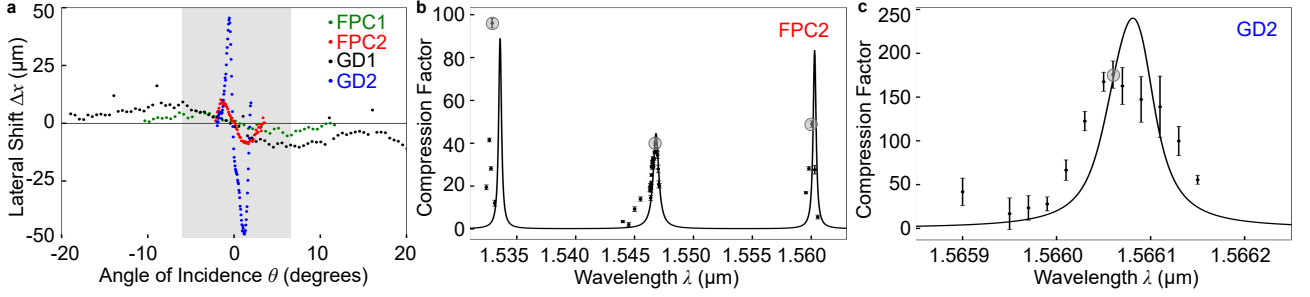


FIG. 4. **Experimentally measured lateral shift and spectral dependence of the compression ratio for the spaceplate devices.** **a.** The lateral shift Δx for four devices was fit to find $\mathcal{R}(\text{GD2}) = 176 \pm 14$ (blue), $\mathcal{R}(\text{FPC2}) = 41.9 \pm 0.6$ (red), $\mathcal{R}(\text{GD1}) = 30 \pm 3$ (black), and $\mathcal{R}(\text{FPC1}) = 3.4 \pm 0.3$ (green). The shaded region indicates the GD2’s angular range from $-\theta_{\text{max}}$ to $+\theta_{\text{max}}$ as an example. **b.** and **c.** The measured compression ratio (solid points) for devices FPC2 and GD2, respectively, for a given input optical wavelength λ along with the compression ratio from the modelled phase response of the multilayer stack (solid black line). The peak measured compression ratio (grey circles) and other characteristic parameter values are given in Table 1.

mission (see SI for details) and the compression ratio over the range of input wavelengths. The device bandwidth is then calculated as the full width at half maximum (FWHM) of the transmission curve.

Table I compiles the performance metrics for all of the spaceplates. The diversity of values in the table demonstrates the freedom of a designer to tailor a multilayer spaceplate for a specific application depending on the desired combination of θ_{max} , bandwidth, and compression ratio. The designs based on gradient descent demonstrated the maximum performance for all three of the latter parameters: GD2 had the highest compression ratio ($\mathcal{R} = 176 \pm 14$), whereas GD1 had both the highest bandwidth (2.8 ± 0.3 nm) and θ_{max} (10°). Tradeoffs between these parameters were evident. For example, the highest compression ratio (GD2) was accompanied by a modest θ_{max} of 1° and the smallest bandwidth of 0.055 ± 0.007 nm of any of the designs. Additionally, the large θ_{max} of GD1 came with a smaller compression ratio, $\mathcal{R} = 60 \pm 4$. A counter-example is that all three measured transmission peaks of device FPC2 demonstrated different compression ratios while retaining the same angular range θ_{max} of

1°. These results show that while there are often tradeoffs between angular range, bandwidth, and compression ratio that need to be considered when targeting a specific spaceplate application [13], these tradeoffs are not universally evident in our devices.

Conclusion

In summary, we fabricated and characterized optical multilayer-stack spaceplates based on two design approaches: grouping layers into coupled resonators and optimizing layer thicknesses via gradient descent. We experimentally demonstrated that these devices can replace free-space propagation up to 176 times their thickness and, when integrated into imaging systems, reduce the distance between the imaging plane and optical components such as lenses. Since they exhibit sharp spectrally peaked responses, multilayer stack-based spaceplates are ideal for narrow-band imaging applications such as LIDAR [20] and retinal scanners. We demonstrated that a spaceplate can cancel the beam walk-off caused by a 260 times thicker glass plate, a feature that would be valuable in optical beam splitters [21] and advanced imaging systems [22, 23]. In this way, our results demonstrate

the potential of spaceplates for miniaturizing imaging systems and advancing flat optics.

Supplementary information accompanies this manuscript.

Methods

The experimental setup is shown in Fig. 7. For all measurements we use a continuous-wave 1.6 mW laser with a wavelength that can be tuned from 1525 nm to 1630 nm with a resolution of 0.1 pm. The beam exits a single-mode fiber and is collimated with an aspheric lens. After passing through a telescope composed of lenses L_1 and L_2 , the beam has a beam width of 0.7 mm. (All L lenses are plano-convex) A quarter-wave plate (QWP), a half-wave plate (HWP) and a polarizing beam-splitter (PBS) are used to set the power of the beam at the spaceplate to $5 \mu\text{W}$. Another QWP and HWP are used after the PBS to set the polarization input to the p -polarization with respect to the spaceplate surface.

Measurement of the lateral beam shift.

To measure the lateral beam shift Δx , we rotate the spaceplate about a vertical axis (i.e., y) using a motorized rotation stage, which varies the angle of incidence θ . To explore the angular range of the spaceplate devices (Fig. 4a), the spaceplate was rotated in steps of 0.05° up to twice the design θ_{\max} in both the positive and negative directions. To determine the compression ratio reported in Fig. 4b and c, the lateral shift was fit over the range of $-\theta_{\max}$ to $+\theta_{\max}$ to retrieve \mathcal{R} for each input wavelength. (Throughout the paper, we quote $1/e^2$ intensity half-widths.)

Since the multilayer devices are of the order of ten microns thick, the lateral shift they create can be small. To measure the shift precisely, we reduce the beam size by focusing the beam with a third lens L_3 with focal length $f_3 = 250$ mm.

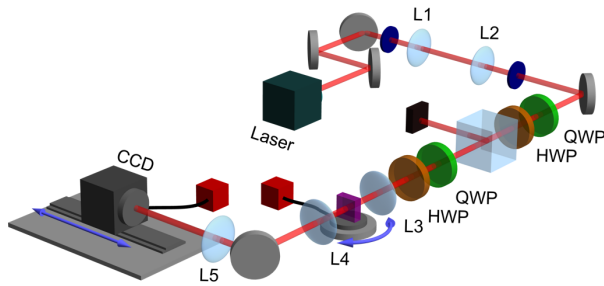


FIG. 5. Experimental setup to measure lateral and focal shifts. A fiber-coupled tunable-wavelength laser creates a beam that is decreased in width by a telescope, lenses L_1 and L_2 . Polarization optics (QWP=quarter-wave plate, HWP=half-waveplate, PBS=polarizing beamsplitter) set the power and polarization of the beam incident on the spaceplate. The beam is focused by lens L_3 onto the spaceplate, which is on a rotation mount to vary the angle of incidence θ . An object plane is imaged onto a camera by a 4-f lens system composed of two lenses, L_4 and L_5 . The camera is translated so as to image different object planes along z after the spaceplate.

The beam's width at the focus is $\omega_0 = 190 \mu\text{m}$ (i.e., the beam waist). The beam passes first through the glass substrate and then the spaceplate multilayer device (nominally, this order should not matter). Note, even with the focusing, the beam's angular width 0.2° is much smaller than any of the devices' designed θ_{\max} .

For each angle θ of the spaceplate, we determine the lateral beam position and, thus, shift Δx by imaging the $x - y$ spatial intensity distribution of the beam. We set the object plane to be the focal plane of the beam, where our precision will be highest. Our imaging system consists of a 4-f telescope composed of lenses L_4 with focal length $f_4 = 100$ mm and L_5 with focal length $f_5 = 150$ mm. The measured magnification was $M = 1.48$. The imaged intensity distribution is measured with an Indium-Gallium-Arsenide (InGaAs) infrared charge-coupled device (CCD) camera ($20 \times 20 \mu\text{m}^2$ pixels, with 320×256 pixels in the horizontal and vertical directions, Bobcat 320 Gig-E). We integrate the $x - y$ spatial intensity distribution over the y direction and then fit to a Gaussian function in x to find the location of the beam center. The difference between this location and the location at normal incidence is the lateral shift, Δx .

Measurement of the focal shift.

To measure the focal shift we image the $x - y$ spatial intensity distribution at different planes along z . To achieve the highest precision measurement of the focal position along z , we decrease the Rayleigh range of the beam by increasing its angular width to 1° by changing lens L_3 to have a focal length $f_3 = 50$ mm. Also to increase precision, we change the imaging system magnification to $M = 5$ by switching L_4 and L_5 to focal lengths of $f = 50$ mm and $f = 250$ mm, respectively. The imaged object-plane is varied along z in increments of 0.04 mm over a range 2 mm by translating the camera with a motorized stage. At each z , we fit the x marginal intensity distribution to a Gaussian to find the beam width ω , as shown Fig. 3a.

The spaceplate in an imaging system.

We observe the action of the spaceplate devices in an imaging system. To do so, we form an image of a lithographic defect in gold using lens L_3 with a focal length $f_3 = 50$ mm and a diameter of 25.4 mm. The z position of L_3 was such that a real image formed after spaceplate location with a magnification of $M = 1.54$ and an NA of 5.57° . We measure the $x - y$ spatial intensity distribution at different z -planes using the same parameters as in the focal measurement. When this z -plane coincides with the plane of the real image, the measured intensity distribution is that of the object, while at other planes it is blurry.

Acknowledgments.

We acknowledge Xiaoqin Gao and Francesco Monticone for scientific discussions, Jordan Pagé for the development of the gradient descent multilayer designs GD1 and GD2, Daniel

Hutama for help with computerized experiment control, and Manuel Ferrer for feedback on the manuscript. This research was undertaken thanks to funding from the Natural Sciences and Engineering Research Council of Canada (NSERC), the Canada Research Chairs Program, and the Canada First Excellence Research Fund.

Author Contributions.

O.R. conceived the experiment; R.H. designed and characterized the samples; B.T.S. and G.C. fabricated the samples; R.H. and O.R. simulated the results; R.H. and Y.M. conducted the experiment; R.H. and Y.M. analyzed the results and drafted the manuscript. J.S.L. and R.W.B. supervised the work. All authors discussed the results and contributed to the text of the manuscript.

-
- [1] Mrnka, Michal, Hendry, Euan, Láčfk, Jaroslav, Lennon, Rachel A., Barr, Lauren E., Hooper, Ian, Phillips, David B., “Space squeezing optics: Performance limits and implementation at microwave frequencies,” *APL Photonics*, vol. 7, no. 7, pp. 076105, 2022.
 - [2] Yu, Nanfang, Capasso, Federico, “Flat optics with designer metasurfaces,” *Nature Materials*, vol. 13, no. 2, pp. 139–150, 2014.
 - [3] Huang, Kun, Qin, Fei, Liu, Hong, Ye, Huapeng, Qiu, Cheng-Wei, Hong, Minghui, Luk’yanchuk, Boris, Teng, Jinghua, “Planar Diffractive Lenses: Fundamentals, Functionalities, and Applications,” *Advanced Materials*, vol. 30, no. 26, pp. 1704556.
 - [4] Liu, Wenwei, Cheng, Hua, Tian, Jianguo, Chen, Shuqi, “Diffractive metalens: from fundamentals, practical applications to current trends,” *Advances in Physics: X*, vol. 5, no. 1, pp. 1742584, 2020.
 - [5] Miyamoto, Kenro, “The Phase Fresnel Lens,” *J. Opt. Soc. Am.*, vol. 51, no. 1, pp. 17–20, 1961.
 - [6] Zhou, You, Zheng, Hanyu, Kravchenko, Ivan I, Valentine, Jason, “Flat optics for image differentiation,” *Nature Photonics*, vol. 14, no. 5, pp. 316–323, 2020.
 - [7] Colburn, Shane, Zhan, Alan, Bayati, Elyas, Whitehead, James, Ryou, Albert, Huang, Luocheng, Majumdar, Arka, “Broadband transparent and CMOS-compatible flat optics with silicon nitride metasurfaces,” *Optical Materials Express*, vol. 8, no. 8, pp. 2330–2344, 2018.
 - [8] Reshef, Orad, DelMastro, Michael P, Bearne, Katherine KM, Alhulaymi, Ali H, Giner, Lambert, Boyd, Robert W, Lundeen, Jeff S, “An optic to replace space and its application towards ultra-thin imaging systems,” *Nature Communications*, vol. 12, no. 1, pp. 1–8, 2021.
 - [9] Guo, Cheng, Wang, Haiwen, Fan, Shanhui, “Squeeze free space with nonlocal flat optics,” *Optica*, vol. 7, no. 9, pp. 1133–1138, 2020.
 - [10] Pagé, Jordan TR, Reshef, Orad, Boyd, Robert W, Lundeen, Jeff S, “Designing high-performance propagation-compressing spaceplates using thin-film multilayer stacks,” *Optics Express*, vol. 30, no. 2, pp. 2197–2205, 2022.
 - [11] Chen, Aobo, Monticone, Francesco, “Dielectric nonlocal metasurfaces for fully solid-state ultrathin optical systems,” *ACS Photonics*, vol. 8, no. 5, pp. 1439–1447, 2021.
 - [12] Díaz-Fernández, Francisco, Máñez-Espina, Luis Manuel, Díaz-Rubio, Ana, Asadchy, Viktor, “Broadband transparent Huygens spaceplates,” *npj Nanophotonics*, 2024.
 - [13] Shastri, Kunal, Reshef, Orad, Boyd, Robert W, Lundeen, Jeff S, Monticone, Francesco, “To what extent can space be compressed? Bandwidth limits of spaceplates,” *Optica*, vol. 9, no. 7, pp. 738–745, 2022.
 - [14] Miller, David AB, “Why optics needs thickness,” *Science*, vol. 379, no. 6627, pp. 41–45, 2023.
 - [15] Sorensen, Nicholas J, Weil, Michael T, Lundeen, Jeff S, “Large-scale optical compression of free-space using an experimental three-lens spaceplate,” *Optics Express*, vol. 31, no. 12, pp. 19766–19776, 2023.
 - [16] Saleh, Bahaa E, Teich, Malvin C, *Fundamentals of Photonics*, Wiley, pp. 313, 1991.
 - [17] McGuirk, Michael, Carniglia, Charles K, “An angular spectrum representation approach to the Goos-Hänchen shift,” *JOSA*, vol. 67, no. 1, pp. 103–107, 1977.
 - [18] Gerken, Martina, Miller, David AB, “Multilayer thin-film structures with high spatial dispersion,” *Applied Optics*, vol. 42, no. 7, pp. 1330–1345, 2003.
 - [19] Klinger, Robert E, Hulse, Charles A, Carniglia, Charles K, Sargent, Robert B, “Beam displacement and distortion effects in narrowband optical thin-film filters,” *Applied Optics*, vol. 45, no. 14, pp. 3237–3242, 2006.
 - [20] Li, Nanxi, Ho, Chong Pei, Wang, I-Ting, Pitchappa, Prakash, Fu, Yuan Hsing, Zhu, Yao, Lee, Lennon Yao Ting, “Spectral imaging and spectral LIDAR systems: Moving toward compact nanophotonics-based sensing,” *Nanophotonics*, vol. 10, no. 5, pp. 1437–1467, 2021.
 - [21] Luo, H, Ren, Z, Shu, W, Li, F, “Construct a polarizing beam splitter by an anisotropic metamaterial slab,” *Applied Physics B*, vol. 87, pp. 283–287, 2007.
 - [22] Engay, Einstom, Huo, Dewang, Malureanu, Radu, Bunea, Ada-Ioana, Lavrinenko, Andrei, “Polarization-dependent all-dielectric metasurface for single-shot quantitative phase imaging,” *Nano Letters*, vol. 21, no. 9, pp. 3820–3826, 2021.
 - [23] Kong, Zheng, Yin, Zhenping, Cheng, Yuan, Li, Yichen, Zhang, Zhen, Mei, Liang, “Modeling and evaluation of the systematic errors for the polarization-sensitive imaging lidar technique,” *Remote Sensing*, vol. 12, no. 20, pp. 3309, 2020.

Supplementary Information

Design and Characterization

The compression factor, \mathcal{R} , is extracted each of the devices comprising the gradient-descent design (GD), and Fabry-Perot cavity design (FPC). The transverse walk-off, Δx , derived from the device transmission phase, ϕ_t , establishes a relationship with the angular dependence of the device.

$$\Delta x = \frac{-1}{k \cos(\theta)} \left(\frac{\partial \phi_t}{\partial \theta} \right)_{\theta_0}, \quad (2)$$

where θ is the incident angle. For any arbitrary optic, the Δx scales with $\tan(\theta)$, however an ideal spaceplate, scales in a negative sinusoidal manner, i.e. Eq. 1 of the main text. The region of linear negative slope dictates the value of \mathcal{R} .

The transmission phase of the device can be determined using transfer-matrix method (TMM) to analyze the multilayer stacks properties as a whole, accounting for its thicknesses and optical properties. Moreover, the transmittance spectrum can be determined for a device to allow further characterization of a device. We simulate the device transmission phase, then fit to an ideal spaceplate phase,

$$\phi_{\text{SP}} = \frac{2\pi n_{\text{BG}}}{\lambda} d_{\text{eff}} \cos(\theta), \quad (3)$$

where $n_{\text{BG}} = n_{\text{air}} = 1$ is the background index, d_{eff} is the effective thickness of the device, and λ is the input wavelength. We can then determine the spectral response of the compression factor, as well as the device numerical aperture. The summary of device characterization is shown in Figure 6.

It can be easily shown that the device, as depicted by its unit cell in Fig. 6d., phase should be quadratic in angle to match an ideal spaceplate, thereby setting a range of angles where the device works, and \mathcal{R} is extracted. The device here has four unit cells. All details of devices and their design parameters can be found in Table II. Fig. 6a. shows a highlighted blue region where the simulated phase fits quadratically to the ideal spaceplate phase, and consequently, sets the operating angular range of the device. Fig. 6b. is the the calculated transverse walk-off. As for the transmittance of the device, the angular and wavelength dependence are shown in Fig. 6c. and e. Then, for each λ used to trace $\Delta x(\theta)$, $\mathcal{R}(\lambda)$ can be deduced, and is shown in Fig. 6f. Notice that transmittance peaks correspond to peaks in compression factor, indicating the resonance type behaviour enhancement of the compression factor.

Measured Device Transmittance

High transmittance is essential for most optical elements used in imaging applications. Figure 6(c) illustrates the transmittance versus input angle for FPC2, showcasing its high transmittance in the highlighted region for a given wavelength. The wavelength chosen is important since it is a resonant effect. While all devices were initially designed to work at $\lambda_{\text{device}} = 1550$ nm, fabrication intolerances shifted the central wavelengths to $\lambda_{m,\text{FPC1}} \approx 1547$ nm, $\lambda_{m,\text{FPC2}} \approx 1531$ nm, $\lambda_{m,\text{GD1}} \approx 1562$ nm, and $\lambda_{m,\text{GD2}} \approx 1567$ nm. The measured

transmittance of each device is shown in Fig. 6. The transmittance of FPC1 is shown in green Fig. 6 containing five peaks. However, we note there are seven peaks due to the criterion of $n - 1$ peaks, where n is the number of unit cells for the FPC designs. Peaks were measured up to 1600 nm highlighting the central peak, where measurements in the main text are taken. FPC2, GD1, and GD2 are shown in red, black, and blue, respectively. The drop in transmittance for GD2 is likely to the large amount of layers, and fabrication intolerances compounding to an overall lower transmittance. From the measured transmittance, we deduce the appropriate range of wavelengths to measure for the compression factor.

Measured Lateral Shift for each FPC2 peak

The FPC designed spaceplate show multiple peaks in transmittance. Through TMM simulations, it was found that the compression factor also peaks at these resonance positions. As seen in Fig. 7, the peak transmittance values of the outer peaks are unequal, indicating a slight difference in the resonance. TMM simulations however indicate symmetric trans-

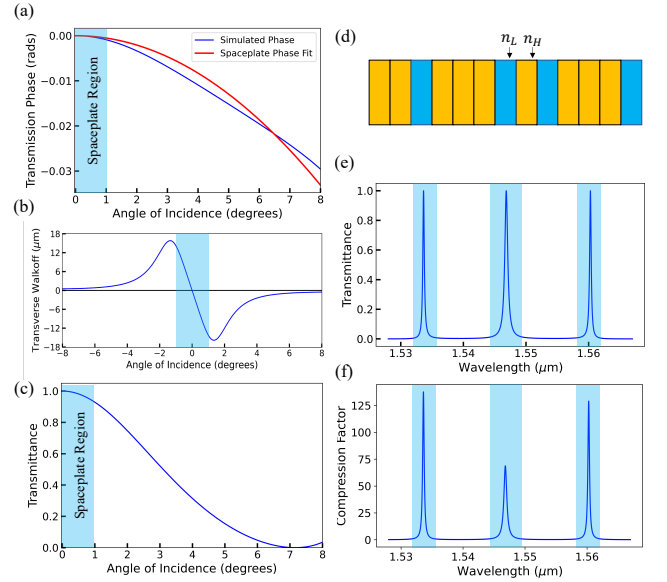


FIG. 6. Characterization of a FPC2 spaceplate. **a.** Calculated TMM transmission phase (blue) is plotted and fit to an ideal spaceplate phase (red) (See. Eq. 3) over the numerical aperture of the device highlighted in light blue. **b.** Calculated lateral shift (transverse walk-off) using Eq. 2. **c.** Angular dependence of transmittance. Approximately constant high transmittance is observed over half the range of the numerical aperture of the device. **d.** Schematic of the unit cell of the FPC2 spaceplate design, as seen in the main text. **e.** Transmittance spectrum showing three ($n - 1$, where $n = 4$ is the number of unit cells) resonance peaks. **f.** Corresponding spectral dependence of the compression factor, \mathcal{R} . Using the fitting method in a. for a given wavelength, the $\mathcal{R}(\lambda)$ can be extracted, showing the similar bandwidth and resonance positions seen in the transmittance in e.

Device	Unit Cell Configuration	Unit Cells	Device Length (μm)	Effective Length (μm)	Compression Factor	Numerical Aperture ($^\circ$)
FPC1	[2L, H, 3L, H]	8	13.10	43.76	3.368	3.5
FPC2	[2L, H, 3L, H, L, H, 3L, H]	4	12.04	767	43.0	1.0
GD1	Gradient Descent	17*	3.55	44.7	18.0	10.0
GD2	Gradient Descent	49*	14.48	3196	238.2	1.0

TABLE II. **Summary of device parameters, performance and configuration.** FPC1 and FPC2 comprise integer-valued multiples of quarter-waves for low and high index layers represented as L and H , respectively, and two other devices of an alternating index, with thicknesses determined by gradient descent. The number of unit cells indicates the repetition count of the unit cell. The compression factor denotes the effective to the real device length ratio. The number of layers is indicated with a star for the gradient descent devices. The device's angular range is also displayed. Note that all devices are quoted for p -polarized light, although s -polarized light exhibits comparable performance in a limited angular range of $\theta_{\text{device}} \leq 10^\circ$.

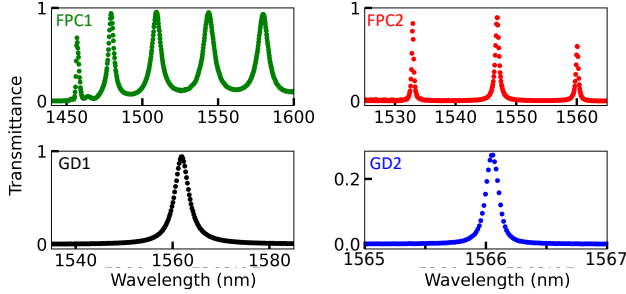


FIG. 7. **Measured transmittance of four devices.** FPC1 and FPC2 show side peaks due to multiple resonances based on integer-valued multiples of $\lambda/4$ layer thickness. Devices GD1 and GD2 show one single resonance peak due to layer thickness based on gradient descent. Designs were simulated using the TMM centred at $\lambda_{\text{device}} = 1550$ nm. Actual wavelengths differ from design wavelength due to fabrication tolerances, therefore $\lambda_{m,\text{FPC1}} \approx 1547$ nm, $\lambda_{m,\text{FPC2}} \approx 1531$ nm, $\lambda_{m,\text{GD1}} \approx 1562$ nm, and $\lambda_{m,\text{GD2}} \approx 1566$ nm. Devices were fabricated on top of 3 mm thick fused silica, with an anti-reflective coating on the films to minimize stress and maximize transmission. The lowest transmittance was measured to be approximately 25% at the peak of device GD2. Transmittance peaks correspond to regions of spatial compression, where the magnitude of spatial compression governs the device's resonance bandwidth and angular range.

mittance about the central resonance. This is due to neglecting the small dispersion of the constituent materials on the wavelength range of interest. Therefore, the dispersion in turn affects the performance of the compression factor as well, showing different slopes for the lateral shift, and consequently \mathcal{R} , as in Fig. 8 for the green and blue curves, corresponding to left and right peaks, respectively. As for the red curve, the compression factor is lower than the outer peaks, and the slope is approximately half of the green curve, leading to a compression factor approximately half of the outer peaks.

Fabrication Details and Analysis

Devices were all designed to thicknesses of approximately $12\mu\text{m}$ or less, except GD1, which was about four times smaller. Devices were grown on fused silica of thicknesses $d = 3.03$ mm for FPC1, FPC2, and GD2, and $d = 2.95$ mm for GD1. Alternating high and low indices comprise silicon ($n_H = 3.2$ at 1550 nm) and silica ($n_L = 1.456$ at 1550 nm), respectively. The films comprising the multilayer stack were deposited using magnetron sputtering. An anti-reflective coating was placed on the device to minimize reflection and counteract any curvature of the sample due to the stress of the films after growth. The device design parameters are summarized in Table II. The device parameters and performance were calculated using TMM.

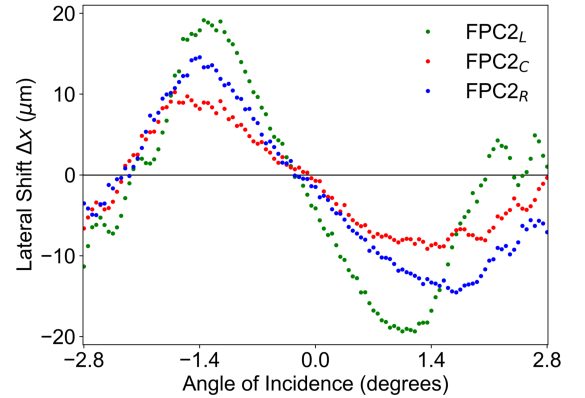


FIG. 8. **Measured lateral shift at FPC2 peak positions.** The lateral shift is measured over two times the numerical aperture of FPC2 at the peak position for each resonance seen in the transmittance spectrum, (See Fig. S2, red curve). The red curve (FPC2_C) indicates the lateral shift for the central peak, with a slope less steep than the outer peaks. Left and right peaks are plotted in green (FPC2_L) and blue (FPC2_R) respectively.